Constructive Interference in Steady State-3DFT MR Imaging of the Inner Ear and Cerebellopontine Angle

Jan W. Casselman,[1] Rudolf Kuhweide,[2] Michael Deimling,[4] Willy Ampe,[2] Ides Dehaene,[3] and Ludo Meeus,[1]

PURPOSE: To assess the value of a three-dimensional Fourier transformation MR technique "CISS" (constructive interference in steady state) in imaging the inner ear. **SUBJECTS:** We studied 50 normal inner ears (40 axial, 10 coronal) and 10 pathologic inner ears in 60 patients. **RESULTS:** The cochlea, semicircular canals, and vestibulum were visualized in detail. Cranial nerve VII and the cochlear, superior vestibular, and inferior vestibular branch of cranial nerve VIII were identified in 90%, 94%, 80%, and 88% of the cases, respectively. A vascular loop was recognized inside the internal auditory canal in 6%, and in the porus in 30%, of the cases. The high signal of the cerebrospinal fluid and labyrinthine fluids (perilymph and endolymph) on the CISS images made excellent delineation of tumors in the cerebellopontine angle and internal canal possible and allowed detection of tumoral labyrinth involvement. The thin sections, high resolution of the images, and capability of producing multiplanar and three-dimensional reconstructions often offered additional information. **CONCLUSIONS:** The CISS sequence allows detailed study of the normal and pathologic inner ear and promises to be highly valuable in the demonstration of the vascular loop.

Index terms: Temporal bone, anatomy; Temporal bone, magnetic resonance; Ear, magnetic resonance; Magnetic resonance, technique.

Computed tomography (CT) has long been the method of choice in the investigation of the labyrinth and internal auditory canal (IAC). With the advent of magnetic resonance (MR) it became clear that MR was superior in the demonstration of soft-tissue structures of the inner ear (1–3); however, two-dimensional Fourier-transformation (2DFT) spin-echo MR techniques provided sections that were 3 mm thick, insufficient for detailed imaging of the inner ear (2, 4), while 3DFT gradient-echo MR studies (1-mm contiguous sections) often lacked good cerebrospinal fluid (CSF)-nerve contrast within the IAC or were very time consuming (1, 2). We present a 3DFT sequence—"constructive interference in steady state" (CISS)—that allows fast and detailed imaging of the inner ear structures and provides excellent CSF-nerve contrast within the IAC and cerebellopontine angle (CPA).

Subjects and Methods

Sixty inner ears were studied using the CISS sequence. In 50 cases (average age of subjects 47 years; 23 men, 27 women), MR was performed for exclusion of acoustic schwannomas (neuromas). An additional CISS sequence was used to study the anatomy of the inner ear only when the routine nonenhanced and gadolinium-enhanced T1-weighted spin-echo images showed no abnormalities. Forty of the 50 CISS studies were done in the axial plane, 10 in the coronal plane. Ten pathologic inner ears (average age of subjects, 47 years; one man, nine women) were also examined with the CISS sequence scheme after the diagnosis had been made with CT and/or MR. Three acoustic schwannomas, one facial nerve schwannoma, one CPA meningioma, one cholesterol granuloma, one glomus jugulare tumor, one case of metastasis in the IAC, one case of fibrous dysplasia, and one case of congenital narrowing (or osteoma formation) of the internal acoustic pore (meatus) (IAP) were studied. In the 50 normal inner ears, visualization of small anatomical structures was checked on the CISS images (Table 1) (Figs. 1A–1G); in particular, visualization of the facial nerve and the cochlear, inferior vestib-

TABLE 1: Reliability of CISS images to show inner ear structures

	40 Inner Ears Axial Plane No./%	10 Inner Ears Coronal Plane No./%
Cochlea	40/100	10/100
Vestibulum	40/100	10/100
LSC-PSC-SSC	40/100	10/100
Internal carotid artery	40/100	10/100
Cranial nerve VII	36/90	9/90
Cochlear branch of nerve VIII	38/95	9/90
Superior vestibular branch of nerve VIII	33/82.5	7/70
Inferior vestibular branch of nerve VIII	36/90	8/80
Anterior segment of facial nerve	39/97.5	7/70
Geniculate ganglion	36/90	5/50
Horizontal segment of facial nerve	34/85	8/80
Posterior genu of facial nerve	23/57.5	8/80
Vertical segment of facial nerve	25/62.5	7/70
Canal of subarcuate artery	26/65	2/20
Vestibular aqueduct	29/72.5	0/

Note.—LSC = lateral semicircular canal, PSC = posterior semicircular canal, SSC = superior semicircular canal.

ular, and superior vestibular branch of cranial nerve VIII was verified, as was the presence of a vascular structure (artery) in the CPA, near or in the IAP or in the IAC (Table 2).

All studies were performed on a 1-T active shielded system (Magnetom SP 42, Siemens, Erlangen, Germany). The use of a standard circular polarized head coil allowed simultaneous imaging of both inner ears. A CISS sequence scheme was used in all cases (5). Fast imaging with steady precession (FISP) and PSIF (mirror sequence of FISP) (contrast-enhanced fast acquisition steady state (CE-FAST)) sequences basically rely on the steady state of both longitudinal and transversal magnetization (6, 7). This steady state is established by excitation of the spin system with radiofrequency pulses at a short repetition time (TR) ≪T2. The development to this state is achieved using a short prescan time of about 1 second before starting the data acquisition itself. As is well known from flow imaging, moving spins will accumulate additional phase shifts when moving along field gradients. If the motion is not constant in time, transverse magnetization will experience random phase shifts and the magnetization may cancel completely (thus completely avoiding a steady state of the transverse magnetization). Therefore, moving cerebrospinal fluid (CSF) does not produce any signal when standard FISP or PSIF sequences are used. (Fig. 2A). Even for very slow flow, the CSF signal may disappear because these flow-induced phase shifts will accumulate over many TR intervals, thus creating a large amount of phase shifts in the magnetization.

Flow compensation techniques have to be used to make sure that spins, independent of their actual velocity, are being refocused. The flow compensation must be applied to each gradient over each TR cycle, unlike standard flow compensation sequences (eg, motion refocusing angiography sequences), in which the flow compensation is applied to the echo. A steady state flow-compensated 3D-FISP

sequence is shown in Figure 3. All three gradients are balanced, indicating that the average value of each gradient is zero. In this case, spins moving at a constant velocity will have the same phase after the application of the gradient pulses as they had before (8). Running a sequence as shown in Figure 3 will produce an image that shows bands of low signal intensity. The occurrence of these bands is not the indication of any system imperfection but is related to basic physical effects. These dark bands are caused by very small magnetic field inhomogeneities and local field distortions due to susceptibility changes that are normally produced by the patient. These inhomogeneities will cause corresponding frequency offsets. If the frequency at a given location is such that the phase angle accumulation over one TR period corresponds to π, or odd integers thereof, the magnetization cancels, and a dark point appears in the image. At another location, the frequency offset might be larger, eg, 2π or a multiple thereof, and the magnetization will interfere constructively, resulting in a high signal intensity at this particular point.

The solution to this inherent problem is to acquire two data sets successively with a "true FISP" (6) sequence of alternating (+−) and nonalternating (++) radiofrequency pulses. The position of the dark bands is shifted in the second data set to the position of high intensity of the first data set. Because of the successive character of data collection, patient movements occurring between the two acquisitions will degrade image quality significantly. An interleaved sequence would destroy the steady state and, therefore, reduce the high CSF-brain contrast. A simple mathematical postprocessing operation (maximum intensity projection (9)) takes the information of each pair of images of the two 3-D data sets created in this way to produce an image with a homogeneous intensity distribution over the whole image and a very good contrast between CSF and nerves (Figs. 1A–1G and 2B). Each data set covers a volume of 32 mm for application in the inner ear. This slab is divided into 32 partitions, resulting in an effective section thickness of 1 mm. The measurement parameters are: TR = 20 msec, TE = 8 msec, matrix size = 256 × 256, field of view = 176 mm and flip angle = 50°. The result is a total acquisition time of 2 times 2.46 minutes and an inplane resolution of each of the 3-D partitions of 0.69 × 0.69 mm. Shim optimization on the patient is not required. A targeted maximum intensity projection on the CISS data set allows also 3-D reconstructed imaging of the inner ear (1) (Fig. 4). The use of a field of view of 176 mm also allows examination of both inner ears when the head coil is used (Fig. 2B). No special hardware requirements will hamper the implementation of this technique. The image quality will benefit from higher field strength. The software is presently available on Siemens 1.0- and 1.5-T systems.

Results

Normal Inner Ears

In the axial plane, the facial nerve was identified in the IAC in 90% of the cases (Figs. 1D, 1F, and
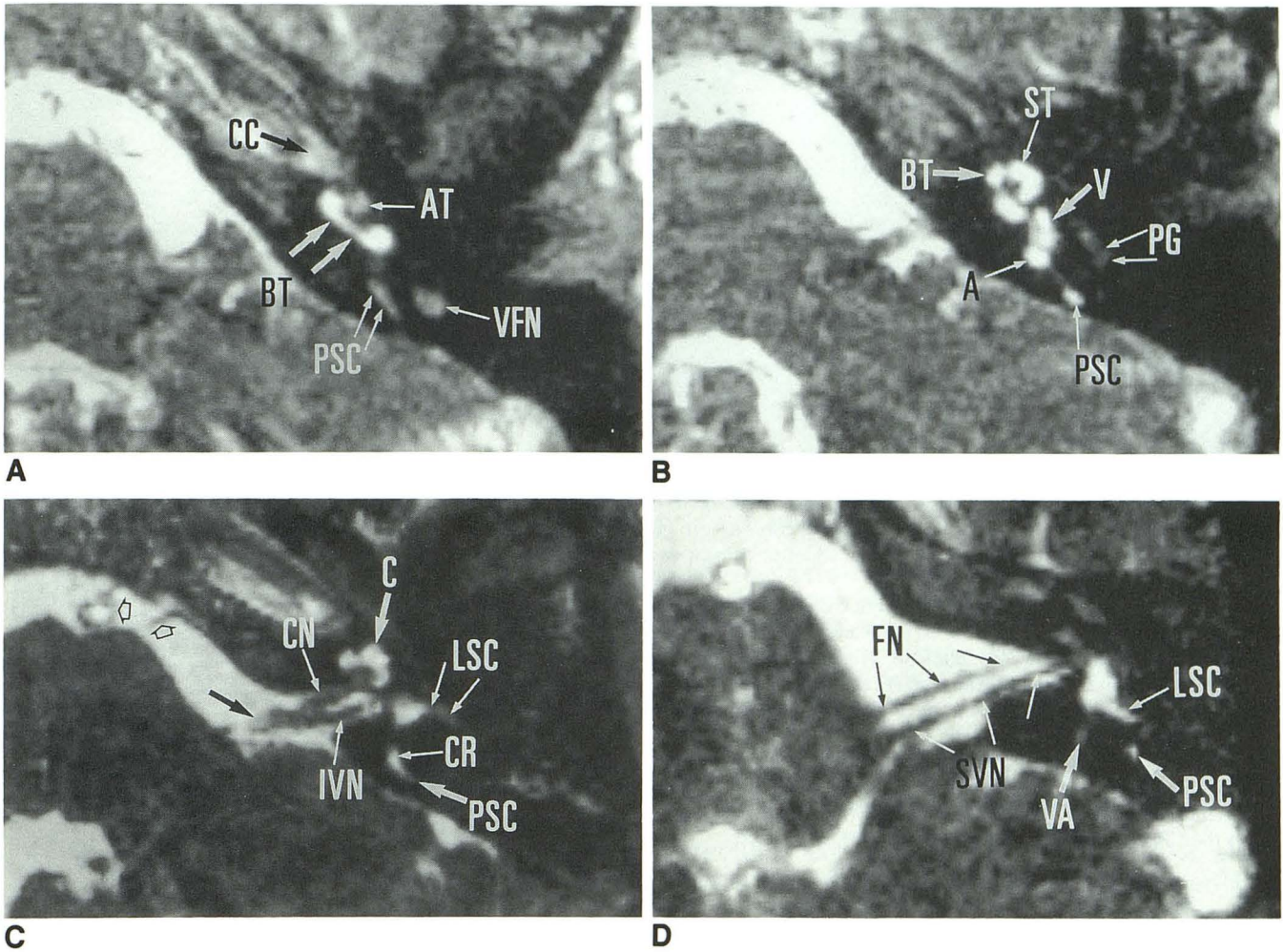
Fig. 1. Axial (*A–E*) and coronal (*F–G*) 1-mm CISS images through a normal left inner ear.

A, Level of basal turn of the cochlea. The high signal inside the posterior semicircular canal (*PSC*), basal turn (*BT*), and apical turn (*AT*) of the cochlea are seen. The vertical segment of the facial nerve is also identified (*VFN*). The carotid artery in the carotid canal is also recognized (*CC*).

B, Level of the utriculosaccular structures. High-signal peri- and endolymph is seen in the basal (*BT*) and second turn (*ST*) of the cochlea, in the utriculosaccular structures (*V*), and in the posterior semicircular canal (*PSC*) and its ampulla (*A*). The posterior genu of the facial nerve (*PG*) has an intermediate signal. The modiolus can be seen as a low-signal structure inside the cochlea.

C, Level of the inferior part of the IAC. Good CSF-nerve contrast makes visualization of the V-shaped bifurcation of the nerve inside the IAC possible and the cochlear branch (*CN*) and inferior vestibular branch (*IVN*) of cranial nerve VIII can be seen. At this level, a part of the posterior semicircular canal (*PSC*) is visible and a part of the crus commune of the superior and posterior semicircular canals (*CR*) is identified. The CSF in the CPA remains high in intensity when the CISS sequence is used in combination with the head coil, making visualization of nerves (*large black arrow*) and vessels (*open black arrows*) in the CSF spaces possible. *LSC*, lateral semicircular canal; *C*, cochlea.

D, Level of the superior part of the IAC. The typical parallel course of the facial nerve (*FN*) and superior vestibular branch of cranial nerve VIII (*SVN*) can be followed throughout the CPA and IAC. The posterior limb of the lateral semicircular canal (*LSC*), the posterior semicircular canal (*PSC*) and the vestibular aqueduct (*VA*) can also be recognized.

1G); the cochlear branch of cranial nerve VIII in 95% (Figs. 1C, 1F, and 1G) of the cases; and the inferior and superior vestibular branch of nerve VIII in 90% and 82.5% of the cases, respectively, (Figs. 1C–1D). In the majority of cases, the anterior segment, geniculate ganglion, and horizontal segment of the facial nerve were visible on the axial images, whereas the posterior genu and the vertical segment were less often visible (Table 1) (Figs. 1A, 1B, 1F, and 1G). The vestibular

aqueduct was identified in 72.5% and the canal of the subarcuate artery in 65% of the cases (Fig. 1E). The basal, second, and apical turn of the cochlea, the vestibulum, all three semicircular canals, and the internal carotid artery were always recognized on the axial and coronal CISS images (Fig. 1).

In the coronal plane, the four nerves were detected in a similar way as in the axial plane (Table 1). The geniculate ganglion of the facial

E

F
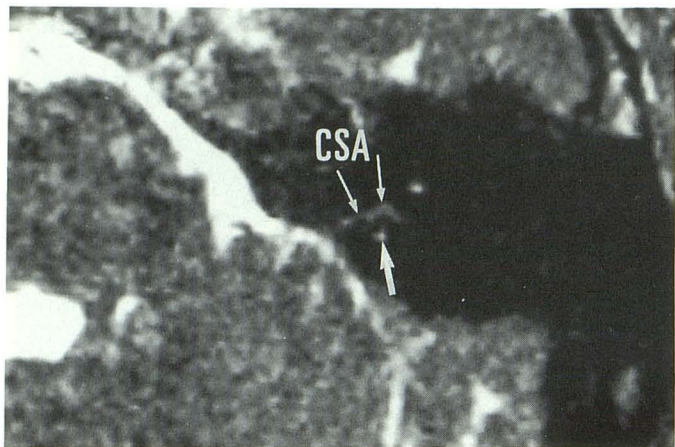
Fig. 1. *Continued. E*, Level of the canal of the subarcuate artery. The visualization of the canal of the subarcuate artery (*CSA*) depends on the size of the canal. The canal can be seen between the anterior and posterior limb of the superior semicircular canal (*large white arrows*).

F, Coronal CISS image through the anterior part of the IAC. The cochlear branch of cranial nerve VIII (*CN*) and the facial nerve (*FN*) can be identified in the coronal plane. The anterior segment of the facial nerve in the bony canal (*AFN*) can also be seen. The bony walls of the internal acoustic pore (*IAP*) are well seen and a part of the cochlea is visible (*C*).

G, Coronal CISS image 1 mm anterior to *F*. The cochlear branch of cranial nerve VIII (*CN*) is seen entering the cochlea (*C*). The anterior segment of the facial nerve (*AFN*) and the vascular loop in the CPA (*large black arrow*) can also be recognized.
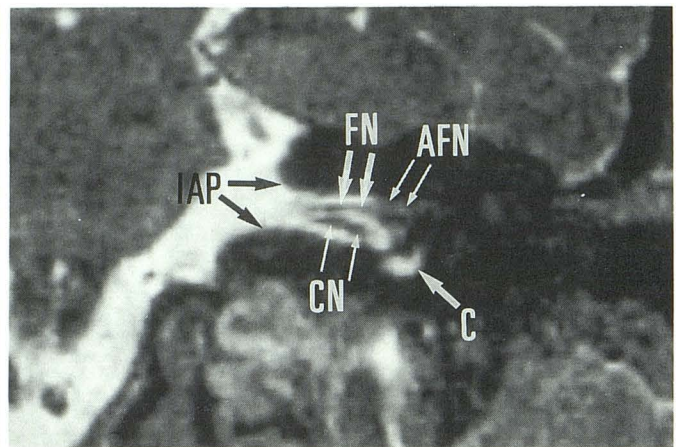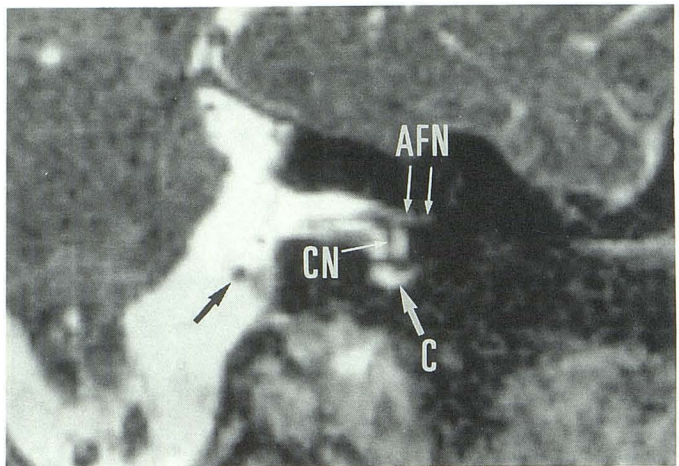
G

TABLE 2: Position of arterial structures (vascular loop) in relation to the CPA, IPA, and IAC

	Axial Plane 40 Inner Ears No./%	Coronal Plane 10 Inner Ears No./%	Total 50 Inner Ears No./%
Vessel in CPA	26/65	6/60	32/64
Vessel near or in IPA	12/30	3/30	15/30
Vessel in IAC	2/5	1/10	3/6

Note.—CPA = cerebellopontine angle, IPA = internal acoustic pore or porus, IAC = internal auditory canal.

nerve was less often visualized, and the posterior genu and vertical segment were more often seen than in the axial plane. It was far more difficult to identify the canal of the subarcuate artery on the coronal images and in the 10 coronal studies no vestibular aqueduct was found.

In 64% of the 50 normal inner ears (coronal and axial plane), a vascular structure was found in the CPA; in 30% of the cases the vessel was present in the IAP; and in 6% of the cases a loop was seen in the IAC (Fig. 5).

Pathologic Inner Ears

All clinical data on the 10 patients that were examined with the CISS sequences are listed in Table 3, including diagnosis, findings during clinical examination, and findings on the CISS images. The major benefits of the CISS sequence scheme—good nerve-CSF contrast in IAC and CPA, good visualization of bony walls due to CSF-bone contrast on thin sections, high in-plane resolution, high intensity of the labyrinthine fluids, ability to make 3-D and multiplanar reconstructions—all contributed to better visualization of the pathology in these cases. Only in one case was the CISS sequence scheme of no benefit at all (case 4).

Discussion

3DFT sequences of the inner ear will only be used when they provide supplementary information and when they are short, so that they can be added to a routine study of the inner ear. Spatial resolution and contrast between different
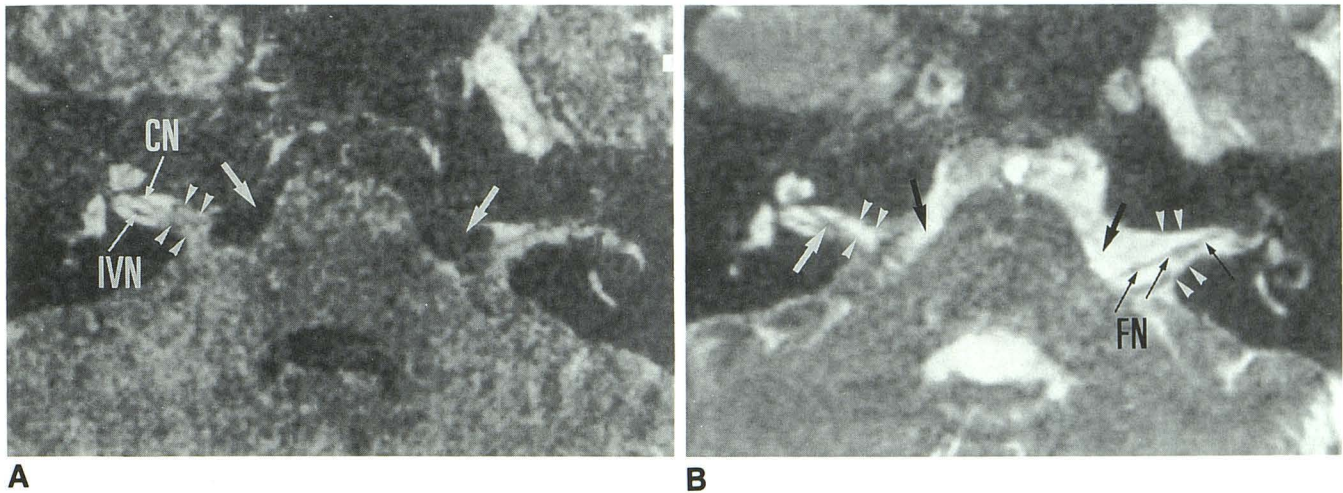
A   **B**

Fig. 2. Axial FISP (A) and CISS (B) images of the same patient through both CPAs and inner ears (same matrix).

A, 1-mm FISP section, 28/10/1 (TR/TE/excitations), angle = 90° and acquisition time = 15 minutes 20 seconds. This 1-mm section shows the cochlear branch (CN) and inferior vestibular branch (IVN) of cranial nerve VIII on the right side but the V-shaped bifurcation is not seen because of signal loss in the medial part of the IAC (white arrowheads). More important CSF flow produces nearly total signal loss in the CPAs (large white arrows). The use of a surface coil can result in more detailed images of the inner ear but will also lead to even more important signal loss in the CPA and near the porus.

B, On this 1-mm CISS image the V-shaped bifurcation of the cochlear and inferior vestibular branch is easily recognized (large white arrow) on the right; there is no signal loss of the CSF in the medial part of the IAC (white arrowheads) or CPA (large black arrows). This makes identification of the facial nerve (FN) throughout the CPA and IAC possible on the left side (small black arrows) (compare with A). Also the inner ear structures are better seen and have a higher signal on this CISS image than on the FISP image.
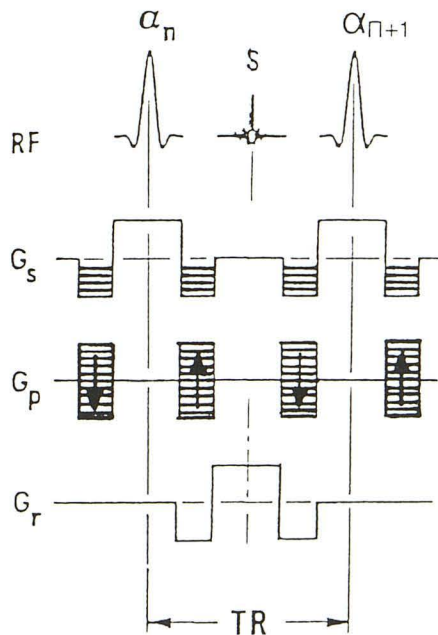

Fig. 3. True FISP 3-D sequence. The three gradients are balanced indicating that the average value of each gradient in the section selection (G_s), phase encoding (G_p), and frequency encoding (G_r) direction is zero. The signal is not flow-refocused at the echo time ($\Phi(s) = 0$, $\Phi(v) \neq 0$) but steady-state refocusing at each TR interval is achieved ($\Phi(s) = 0$, $\Phi(v) = 0$). This is sufficient to retain the high signal for slow motion. High flows (eg, vessels) are depicted as hypointense zones. This true FISP sequence is repeated twice when the CISS sequence scheme is used, once with nonalternating radiofrequency ($\alpha_h = \alpha_{n+1} = \alpha^{++}$) and once with alternating radiofrequency ($\alpha_n = \alpha_{n+1} = \alpha^{+-}$).

structures are also important (1, 4). Our study shows that the CISS sequence scheme enables us to obtain high-resolution images with good contrast between CSF and nerves (Figs. 1 and 2). Consequently, the reliability of this sequence to show the four nerves within the IAC separately is high. The most difficult nerve to visualize was the superior vestibular branch of cranial nerve VIII, which was often difficult to separate from the inferior vestibular branch. One of the reasons these nerves cannot always be separated is because we used the head coil and studied both inner ears simultaneously, so that images perfectly parallel to the IAC could not always be achieved. Another reason is that in very narrow IACs the nerves are closer together and less CSF is present, so that the spatial resolution can become critical (10) and the high CSF-nerve contrast is lost. In these circumstances, one has to rely on the typical anatomical pattern of the nerves to distinguish them from one another.

On axial images, the inferior vestibular branch and the cochlear branch of cranial nerve VIII can be seen as a V-shaped bifurcating nerve in the distal half of the IAC (Figs. 1C, 2B, and 5A). The superior vestibular branch of cranial nerve VIII and cranial nerve VII can be seen as parallel structures throughout the total length of the IAC (10, 11) (Fig. 1D). It is important to use the head
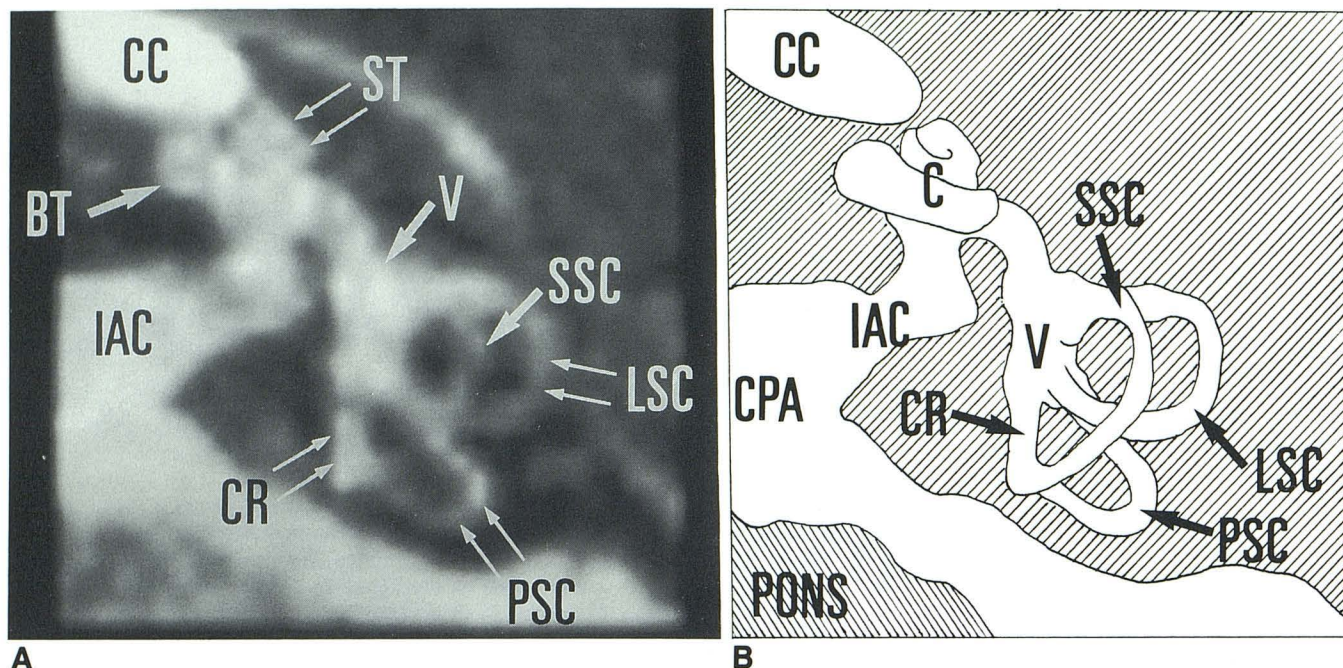
A   **B**

Fig. 4. 3-D reconstruction of the left cochlea and labyrinth reconstructed from an axial 3DFT-CISS data set, craniocaudad view (A) and corresponding drawing (B). Simultaneous visualization of the total membranous labyrinth including basal (BT) and second/apical (ST) turn of the cochlea, utriculosaccular structures (V), superior (SSC), lateral (LSC), and posterior (PSC) semicircular canals, common crus (CR) of posterior and superior semicircular canals is possible only on 3-D reconstructions. IAC, internal auditory canal; CC, carotid artery in carotid canal; CPA cerebellopontine angle.

coil. Surface coil imaging provides good images of the labyrinth but there is a rapid loss of signal in the deeper regions, resulting in loss of contrast between CSF and nerves, especially in the CPA and proximal IAC. But the high signal of the CSF in the CPA is also lost due to CSF flow, as is the case when FISP sequences are used (Fig. 2A). The very high signal of the intralabyrinthine fluid on CISS images is reflected in the 100% reliability in visualizing the structures of the labyrinth. The weakness of the CISS sequence scheme is the lack of contrast between soft tissues and even between soft tissues and bone. This weakness explains the inconstant identification of the facial nerve, especially in the vertical segment and posterior genu, where only bone and no endolymph is present adjacent to the nerve. For the same reason, the canal of the subarcuate artery is less frequently seen. This canal can also be very thin so that the spatial resolution can pose a problem.

The better identification of the vestibular aqueduct on axial images (Figs. 1D, 5B, and 5C) than on coronal images is explained by the parasagittal orientation of the aqueduct. The vascular supply of the labyrinth is derived from the anterior inferior cerebellar artery in 80% of cases, from the

accessory anterior cerebellar artery in 17%, and from the posterior inferior cerebellar artery in 3% of the cases (12). CISS images often show an artery in the CPA cistern (64% of cases), in or near the porus (30% of cases), and in the IAC (6% of cases) (Figs. 5A–5C). On these images not only are the vessels seen, but the relation of the vessels to the cranial nerves VII and VIII are also appreciated. Therefore, 3DFT MR could well replace angiography and air CT cisternography in the diagnosis of cross-compression of the vestibular nerve by the arterial loop in patients with intractable vertigo or motion intolerance. Mazzoni reported a vascular loop inside the IAC in 40% and near the porus in 37% of cases (13). Other authors mention that the convexity of the loop is seen in the porus or enters the IAC in 40%–67% of the cases (14), correlating better with our findings on the CISS images.

In case of pathology of the inner ear, CISS images often provided additional information (Table 3). Gadolinium-enhanced T1-weighted images remain necessary; the diagnosis of labyrinthitis, neuritis, tumoral invasion of nerves (case 8), and meningeal involvement (case 5) cannot be made or are more difficult to make without the use of gadolinium (15, 16). On the other hand,
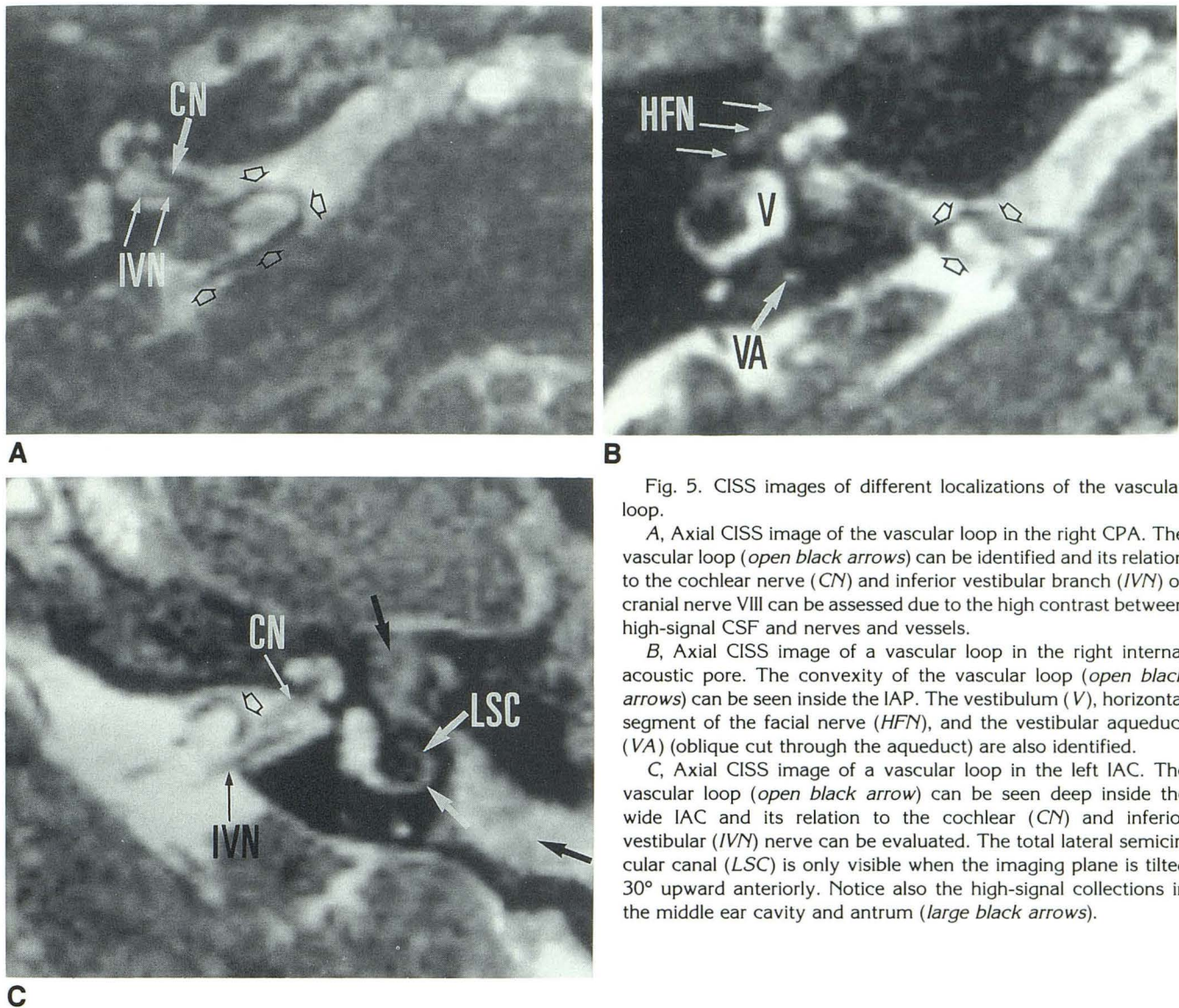
A

B

C

Fig. 5. CISS images of different localizations of the vascular loop.

A, Axial CISS image of the vascular loop in the right CPA. The vascular loop (*open black arrows*) can be identified and its relation to the cochlear nerve (*CN*) and inferior vestibular branch (*IVN*) of cranial nerve VIII can be assessed due to the high contrast between high-signal CSF and nerves and vessels.

B, Axial CISS image of a vascular loop in the right internal acoustic pore. The convexity of the vascular loop (*open black arrows*) can be seen inside the IAP. The vestibulum (*V*), horizontal segment of the facial nerve (*HFN*), and the vestibular aqueduct (*VA*) (oblique cut through the aqueduct) are also identified.

C, Axial CISS image of a vascular loop in the left IAC. The vascular loop (*open black arrow*) can be seen deep inside the wide IAC and its relation to the cochlear (*CN*) and inferior vestibular (*IVN*) nerve can be evaluated. The total lateral semicircular canal (*LSC*) is only visible when the imaging plane is tilted 30° upward anteriorly. Notice also the high-signal collections in the middle ear cavity and antrum (*large black arrows*).

in case of acoustic schwannoma, CISS images allow exact measurement of the tumor size without the use of gadolinium (cases 1–3). The relation of the schwannoma to the CPA and porus is best seen on CISS images because of the high signal of the CSF in the CPA cistern and the easily recognized bony porus borders and bony IAC walls (Fig. 6). The bony structures are more difficult to evaluate when only routine spin-echo images are used; often CT was required to make bone evaluation possible. Extension of other tumors in the CPA cistern (cases 5–8) can also be seen on CISS images.

3DFT-CISS images can also play a role in the differential diagnosis between acoustic schwan-

noma and other tumors. When cranial nerves VII and VIII can be seen coming out of a tumor in a perpendicular way, then an acoustic schwannoma is unlikely (case 5) (Fig. 7). The thin adjacent sections make it possible to see thin structures or lesions. The small fistula between the cholesterol granuloma and the posterior semicircular canal (case 6) and the connection between the CPA meningioma and the small meningioma extension in the gasserian ganglion (case 5) were recognized only on the CISS images. Thin adjacent sections are also suited to make reconstructions in other planes, which can often add important information (case 10) (Fig. 8). The high signal of the intralabyrinthine fluids on the CISS images

TABLE 3: Clinical findings and findings on CISS images in 10 patients with inner ear pathology

Case	Age/Sex	Diagnosis/Affected Side	Clinical Findings	Findings on CISS Images	Contribution of CISS
1	62/F	Acoustic schwannoma/L	SNHL, abnormal ABR	12 × 18 mm lesion centered on porus with widening of the porus	Evaluation relation tumor-IAC walls, evaluation of extension in CPA
2	62/F	Acoustic schwannoma/L	Disequilibrium	Mass in IAC, extension in CPA	Delineation tumor versus IAC walls and CPA, CSF, and structures
3	78/F	Acoustic schwannoma/L	SNHL, abnormal ABR	10 × 4 mm mass inside IAC, normal porus	Evaluation of relation tumor-IAC walls, normal porus
4	35/M	Facial nerve schwannoma/L	Facial nerve palsy	Enlargement of geniculate ganglion	
5	71/F	CPA meningioma/L	Vertebrobasilar ischemic disease symptoms	Lesion in CPA, extension to gasserion ganglion	Visualization of connection between lesion in CPA and in gasserion ganglion, shows nerves perpendicular to the mass
6	30/F	Cholesterol granuloma/L	SNHL in the low frequency range	Lesion in bony labyrinth, fistulization to PSC	Visualization of fistula
7	41/F	Recurrent glomus jugulare tumor/L	Mixed hearing loss	Glomus tumor with involvement of bone around PSC, PSC remains intact	Confirmation of intact membranous labyrinth
8	60/F	Breast carcinoma metastasis/L	Facial pain, facial nerve palsy	Tumor in CPA, IAC, and geniculate ganglion	Delineation of tumor versus CSF in CPA
9	15/F	Fibrous dysplasia/R	Disequilibrium, conductive hearing loss, temporal-occipital-parietal skull deformities	Bone alterations, IAC-V-semicircular canal involvement	Shows involvement of membranous labyrinth (3-D reconstructions)
10	22/F	Presumed congenital stenosis or osteomas IAP/L + R	SNHL, abnormal ABR	Narrow IAPs	Evaluation bony IAP, 3-D data allowed multiplanar reconstruction

Note.—L = left, R = right, ABR = auditory evoked brain-stem responses, CPA = cerebellopontine angle, CSF = cerebrospinal fluid, IAC = internal auditory canal, IAP = internal acoustic pore (meatus), PSC = posterior semicircular canal, SNHL = sensorineural hearing loss, V = vestibulum.


A

B

C
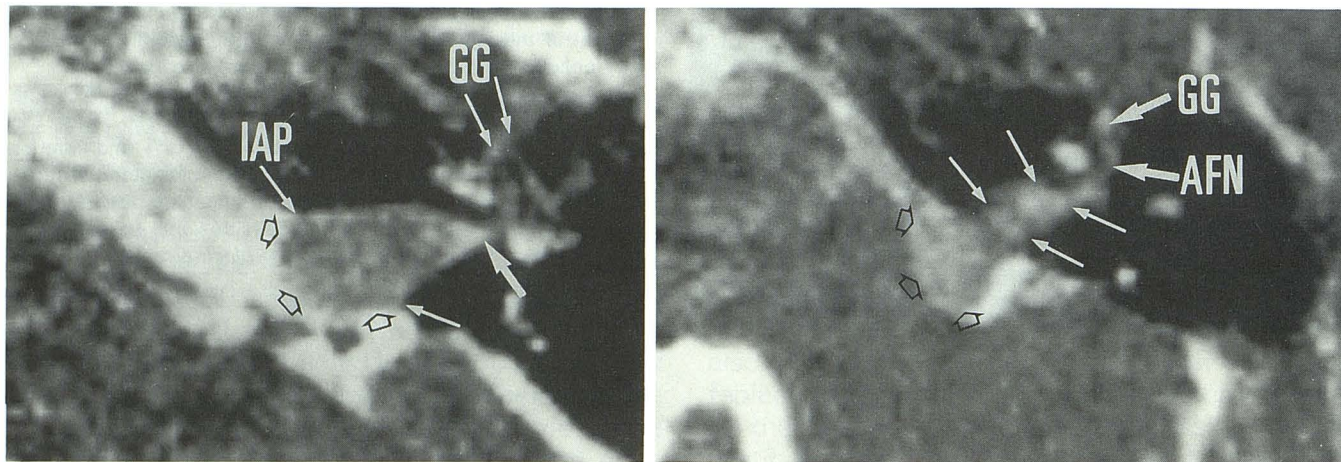
Fig. 6. CISS imaging of acoustic schwannomas, axial images through the IAC.

A, Acoustic schwannoma centered on the left IAP (case 1). Extension of the schwannoma in the CPA (*open black arrows*) and widening of the internal acoustic pore (*IAP*) (*small white arrows*) can be evaluated due to the high tumor-CSF-bone contrast and high resolution. Even CSF entrapped near the fundus of the IAP can be seen (*large white arrow*). Notice also the geniculate ganglion (*GG*).

B, Acoustic schwannoma filling up the total left IAC (*small white arrows*) with extension in CPA and lying against the brain stem (*open black arrows*) (case 2). GG, geniculate ganglion; AFN, anterior segment of the facial nerve.

C, Acoustic schwannoma completely inside the left IAC (case 3). The schwannoma surrounded by a thin layer of CSF (*large white arrows*) produces only widening of the middle part of the IAC. The normal porus (*IAP*) and CSF in the CPA near the porus (*open black arrow*) can be seen.
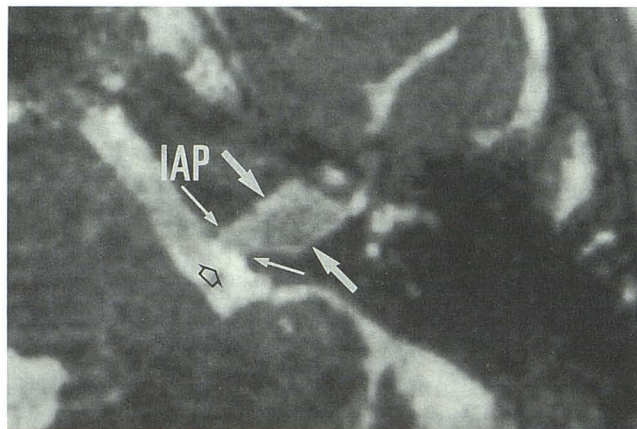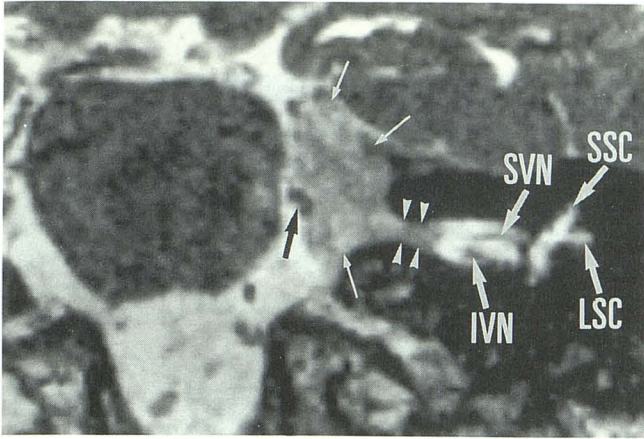
Fig. 7. Seventy-one-year-old woman with meningioma in the left CPA (case 5), coronal CISS image. A large meningioma (*small white arrows*) is seen in the CPA with extension in the IAC (*white arrowheads*). The porus is not enlarged and the tumor is attached to the tentorium. The superior (*SVN*) and inferior (*IVN*) vestibular branch of cranial nerve VIII can be seen coming out of the mass in a perpendicular way, making the diagnosis of acoustic schwannoma unlikely. The vascular loop is displaced medially (*black arrow*). *SSC*, superior semicircular canal; *LSC*, lateral semicircular canal.
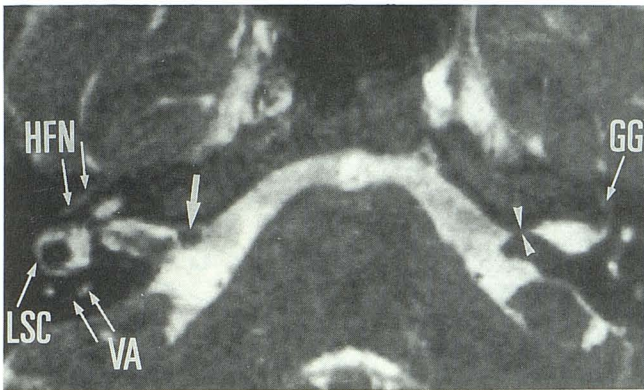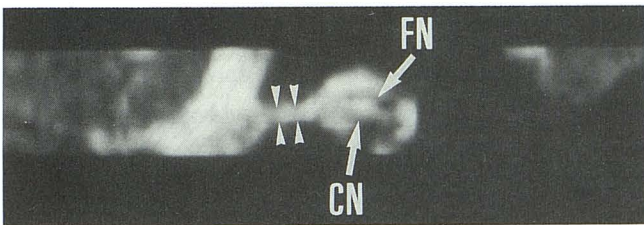
Fig. 8. Twenty-two-year-old woman with presumed congenital stenosis of the porus or osteomas of the porus on both sides (case 10). Axial CISS image (*A*) and coronal reconstruction (*B*).

A, The extreme narrowing of the left porus (*white arrowheads*) is easily recognized due to the high CSF-bone contrast. A calcification (presumed osteoma) is narrowing the right porus (*large white arrow*). The horizontal segment of the facial nerve (*HFN*), the total lateral semicircular canal (*LSC*), and the vestibular aqueduct (*VA*) are recognized on the right side. *GG*, geniculate ganglion.

B, The coronal reconstruction through the left IAC confirms the narrowing of the porus (*white arrowheads*) and the spatial and contrast resolution of the reconstruction is good enough to recognize the facial nerve (*FN*) and the cochlear branch of the vestibular nerve (*CN*).
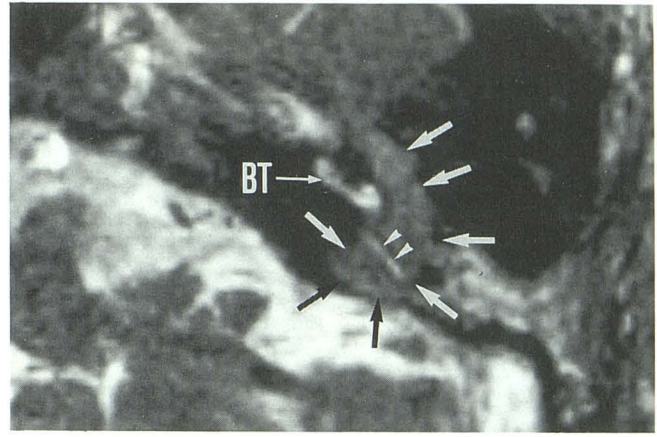

Fig. 9. Recurrent glomus jugulare tumor in 41-year-old woman (case 7). Axial CISS image through the left inner ear. The tumor is seen in the middle ear cavity and in the inner ear with destruction of bone around the posterior semicircular canal (*large arrows*). This CISS image indicates that the membranous labyrinth is still intact and shows the high signal of the endolymph inside the posterior semicircular canal (*white arrowheads*). CT remains, of course, the first study to evaluate bone destruction, but CISS images can detect more reliably obliteration of the endo- and perilymph spaces (also uncalcified obliteration) and, at the same time, allow good evaluation of bone destruction. *BT*, basal turn of cochlea.

makes it possible to detect or exclude involvement of the membranous labyrinth (cases 7–9) (Fig. 9).

Another advantage of the high signal of the endolymph-perilymph and the high contrast with the surrounding bony labyrinth on CISS images is that these images can be used to make 3-D membranous labyrinth reconstructions (1) (Fig. 10). Narrowing or obliteration of the endolymph spaces can be detected (case 9) (Figs. 9 and 10). Finally, the weak contrast between soft-tissue lesions and surrounding bone can leave the lesions invisible on CISS images. This is certainly the case in parts of the inner ear where no or little CSF or intralabyrinthine fluid is present, as around the segments of the facial nerve located in the facial canal (cases 4 and 8).

In conclusion, the CISS sequence scheme allows reliable imaging of the labyrinth structures and the nerves inside the CPA and IAC. Localization of the vascular loop in relation to the CPA, porus, or IAC is also promising. Additional information can be achieved when pathologic inner ears are studied with the CISS sequence scheme. Therefore, this short sequence was added to our routine inner ear protocol.

Acknowledgments

A

B

C
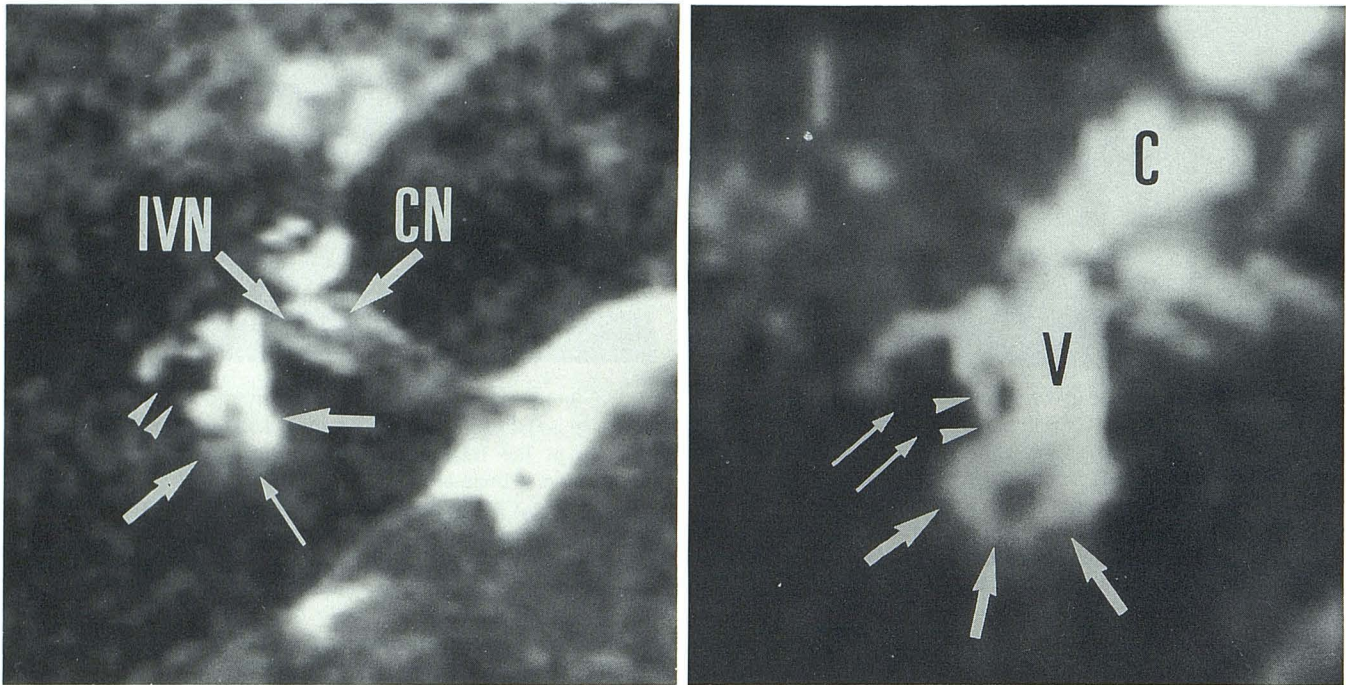
Fig. 10. Fifteen-year-old girl with fibrous dysplasia of the right temporal bone (case 9). Axial CISS image (*A*) and 3-D reconstruction of the right labyrinth (*B*) and drawing of *B* (*C*).

A, Involvement of the labyrinth in case of fibrous dysplasia is very rare. Unsharp delineation of the posterior part of the vestibulum and interruption of normal endolymph spaces in crus communis of posterior and superior semicircular canal (*large white arrows*), posterior limb of lateral semicircular canal (*white arrowheads*), and in ampulla and inferior part of the posterior semicircular canal (*small white arrow*) is seen. The labyrinth involvement was also confirmed on CT images. *IVN*, inferior vestibular nerve; *CN*, cohlear nerve.

B, On this craniocaudad oriented 3-D reconstruction of the right labyrinth, all three semicircular canals should be visible (see Fig. 4). This image shows definite interruption of the lateral semicircular canal (*small white arrows*). The posterior delineation of the endolymph in the posterior semicircular canal is irregular (*large white arrows*) and impression on the superior semicircular canal can be presumed (*white arrowheads*). Partial visualization of the lateral semicircular canal on Figure 1A could have been produced by an oblique cut through the canal but the 3-D reconstruction proves that this was not the reason and that a real interruption of the canal is present. *C*, cochlea; *V*, vestibule.

C, The lateral semicircular canal is interrupted (*large black arrows*), the posterior semicircular canal has an irregular posterior delineation (*open black arrows*), and an impression is seen on the superior semicircular canal (*black arrowheads*). The vestibule (*V*) and cochlea (*C*) are normal. *CC*, carotid artery in carotid canal; *IAC*, internal auditory canal.
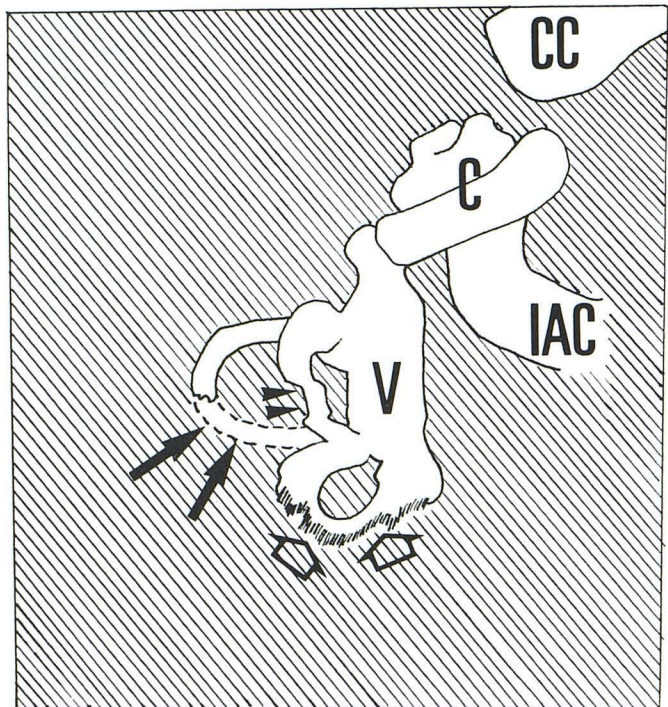
References

1. Tanioka H, Shirakawa T, Machida T, Sasaki Y. Three dimensional reconstructed MR imaging of the inner ear. *Radiology* 1991;178:141–144

2. Brogan M, Chakeres DW, Schmalbrock P. High-resolution 3DFT MR

imaging of the endolymphatic duct and soft tissues of the otic capsule. *AJNR* 1991;12:1–11

3. Tanioka H, Machida T, Zusho H. High resolution MRI of the temporal bone using a surface coil: normal anatomy. *Jpn J Med Imaging* 1989;8:2–8

4. Enzmann D, O'Donohue J. Optimizing MR imaging for detecting small tumors in the cerebellopontine angle and internal auditory canal. *AJNR* 1987;8:99–106

5. Deimling M, Laub GA. Constructive interference in steady state for motion sensitivity reduction (abstr). In: Book of abstracts: Society of Magnetic Resonance in Medicine 1989. Vol 1. Berkeley, CA: Society of Magnetic Resonance in Medicine, 1989:842

6. Gyngel ML, Palmer ND, Eastwood LM. The application of steady state free precession (SSFP) in 2DFT MR imaging (abstr). In: Book of abstracts: Society of Magnetic Resonance in Medicine 1986. Vol 3. Berkeley, CA: Society of Magnetic Resonance in Medicine 1986:666

7. Oppelt A, Graumann R, Barfuss H, Fischer H, Hartl W, Schajor W. FISP, a new fast MRI sequence. *Electromedica* 1986;54:15–18

8. Patz S. Some factors that influence the steady state in "steady state" free precession. *Magn Reson Imaging* 1988;6:405–413

9. Laub GA, Kaiser WA. MR angiography with gradient motion refocusing. *J Comput Assist Tomogr* 1988;12:377–382

10. Valvassori GE, Morales FG, Palacios E, Dobben GE. MR of the normal and abnormal internal auditory canal. *AJNR* 1988;9:115–119

11. Daniels DL, Haughton VM. The temporal bone. In: Daniels DL, Haughton VM, Naidich TP, eds. *Cranial and spinal magnetic resonance imaging: an atlas and guide*. New York: Raven, 1987:197–234

12. Bergeron RT, Lo WW, Swartz JD, Hasso AN, Liu D, Broadwell RE. The temporal bone. In: Som PM, Bergeron RT, eds. *Head and neck imaging*. 2nd ed. St. Louis: Mosby, 1991:925–1115

13. Mazzoni A. Internal auditory canal: arterial relations at the porus acusticus. *Ann Otol* 1969;78:797–814

14. Esfahani F, Dolan K. Air CT cisternography in the diagnosis of vascular loop causing vestibular nerve dysfunction. *AJNR* 1989;10:1045–1049

15. Seltzer S, Mark AS. Contrast enhancement of the labyrinth on MR scans in patients with sudden hearing loss and vertigo. *AJNR* 1991;12:13–16

16. Brogan M, Chakeres DW. Gd-DTPA-enhanced MR imaging of cochlear schwannoma. *AJNR* 1990;11:407–408